Giant Plasmene Nanosheets, Nanoribbons, and Origami

Kae Jye Si,[†,‡,▽] Debabrata Sikdar,[§,▽] Yi Chen,[†,‡] Fatima Eftekhari,[‡] Zaiquan Xu,[⊥] Yue Tang,[†,‡] Wei Xiong,[†,‡] Pengzhen Guo,[†,‡] Shuang Zhang,[∥] Yuerui Lu,[∥] Qiaoliang Bao,[#,⊥] Weiren Zhu,[§] Malin Premaratne,[§] and Wenlong Cheng*[,†,‡]

[†]Department of Chemical Engineering, Faculty of Engineering, Monash University, Clayton 3800, Victoria, Australia, [‡]The Melbourne Centre for Nanofabrication, 151 Wellington Road, Clayton 3168, Victoria, Australia, [§]Advanced Computing and Simulation Laboratory (AχL), Department of Electrical and Computer Systems Engineering, Faculty of Engineering, Monash University, Clayton 3800, Victoria, Australia, [⊥]Department of Materials Engineering, Faculty of Engineering, Monash University, Clayton 3800, Victoria, Australia, [∥]Research School of Engineering, College of Engineering and Computer Science, Australian National University, Canberra 0200, Australian Capital Territory, Australia, and [#]FUNSOM and Collaborative Innovation Center of Suzhou Nano Science and Technology, Soochow University, Suzhou 215123, P. R. China. [▽]These authors contributed equally.

ABSTRACT We introduce *Plasmene*— in analogy to graphene—as free-standing, one-particle-thick, superlattice sheets of nanoparticles ("meta-atoms") from the "plasmonic periodic table", which has implications in many important research disciplines. Here, we report on a general bottom-up self-assembly approach to fabricate giant plasmene nanosheets (*i.e.*, plasmene with nanoscale thickness but with macroscopic lateral dimensions) as thin as ~40 nm and as wide as ~3 mm, corresponding to an aspect ratio of ~75 000. In conjunction with top−down lithography, such robust giant nanosheets could be milled into one-dimensional nanoribbons and folded into three-dimensional origami. Both experimental and theoretical studies reveal that our giant plasmene nanosheets are analogues of graphene from the plasmonic nanoparticle family, simultaneously possessing unique structural features and plasmon propagation functionalities.

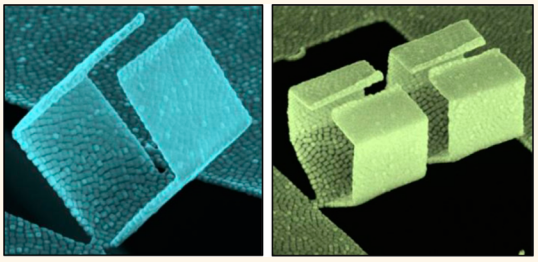

KEYWORDS: self-assembly · giant · plasmene · nanosheet · nanoribbon · origami · graphene

Although the past two decades have witnessed the emergence of various superlattice materials from quantum dots,[1−3] magnetic[2,4,5] and metal[6−23] nanoparticles, and even protein,[24] their plasmonic properties did not draw much attention until recently.[11,25−27] Plasmon hybridization theory[28] predicts the resonance coupling in structurally well-defined nanoparticle assemblies including plasmonic molecules, polymers, two-dimensional (2D) and three-dimensional (3D) superlattices.[29] In particular, for free-standing plasmonic nanoparticle superlattice sheets (termed plasmene), the hybridized plasmon modes and near-field distributions can be strictly controlled in a 2D plane, which can in principle be programmed by adjusting the sizes and shapes of the constituent nanoparticles and varying the interparticle spacing (note that porous metallic sheets were previously defined as plasmene rolls;[30] however, our plasmene is built from elemental nanoparticle building blocks, a true analogue to graphene). The ability to fabricate plasmene nanosheets is of fundamental significance for understanding the large-scale 2D self-assembly, and of practical significance for engineering of flexible/stretchable plasmonic devices and circuits. Despite a few recent examples of free-standing plasmonic nanoparticle superlattices,[5,11,16,27,31] none of them can meet the requirement of giant plasmene nanosheets, let alone further manufacturing into 1D or 3D plasmonic structures. Using bimetallic Au@Ag nanocubes (NCs) as model building blocks, we demonstrate a general self-assembly approach to fabricate giant plasmene nanosheets, which can be further shaped into nanoribbons and origamis in conjunction with top−down focused ion beam (FIB) lithography.

RESULTS AND DISCUSSION

We begin with synthesis of monodisperse Au@Ag NCs by following the recently reported protocols[32] with some minor modifications. In brief, gold nanospheres with diameter of ~11 nm were synthesized and

* Address correspondence to wenlong.cheng@monash.edu.

Received for review August 17, 2014 and accepted September 29, 2014.

Published online September 29, 2014
10.1021/nn504615a

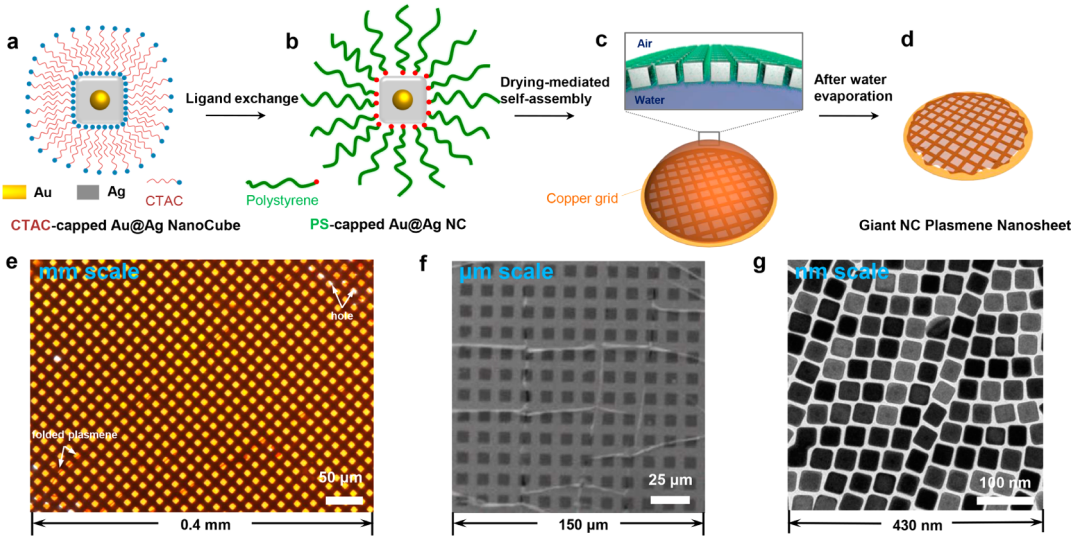

Figure 1. Fabrication of giant NC-plasmene nanosheets. (a–d) Schematic of fabrication process of NC-plasmene nanosheets by ligand exchange in conjunction with drying-mediated self-assembly. Characterization of giant NC-plasmene nanosheets at the (e) macro-, (f) micro-, and (g) nanoscale by optical microscope, SEM, and TEM, respectively.

used as cores, and a uniform coating layer of silver was deposited on them. The average edge lengths of the as-synthesized NCs can be tuned from ~21 to ~33 nm. Such NCs exhibit well-pronounced dipolar, quadrupolar and octopolar localized surface plasmon resonance (LSPR) bands[33] (see Supporting Information Figures S1 and S2). Notably, the pristine NCs were stabilized by hexadecyltrimethylammonium chloride (CTAC), a weak-binding ligand, which nevertheless provides insufficient protection from random nanoparticle aggregation. Therefore, a two-step ligand exchange procedure[27,31] was applied to replace CTAC by a much stronger binding ligand, thiolated-polystyrene (PS) (M_n = 50 000 g mol^{-1}) (Figure 1).

To grow giant plasmene nanosheets, a droplet of concentrated chloroform solution of PS-capped NCs was spread onto a sessile water drop on a holey copper grid (2000 mesh with hole-size of 7 μm × 7 μm, Figure 1c). Rapid chloroform evaporation confined the self-assembly of PS-capped NCs at the air/water interface forming monolayered nanosheet patches. Subsequent slow water evaporation reduced the interface area by about 50% from a hemisphere-like surface to a pancake-like surface. This process gradually fused the patchy nanosheets into giant nanosheets covering the entire holey substrate. Such-formed plasmene sheets could have a lateral dimension of ~3 mm and a thickness of ~40 nm, corresponding to an aspect ratio of ~75 000.

At the macroscopic scale, the plasmene sheets were readily observable under an optical microscope with distinct colors (Figure 1e); at the microsocopic scale, the plasmene sheets were monolayered yet flexible (Figure 1f); at the nanoscopic scale, NCs were in ordered packing (Figure 1g). The quality of giant plasmene nanosheets critically depended on the length of the polymer ligands but was almost independent of the type of substrates. Strikingly, our giant plasmene nanosheets could be even shaped into desired shapes and patterned into regular arrays. Atomic force microscope (AFM) line scanning further proved that our plasmene nanosheets were single-particle-thick, with an average thickness of 40 ± 2 nm. Despite being extremely thin, the sheets were mechanically strong, with a typical Young's modulus of ~1 GPa, as derived from the AFM nanoindentation (see Supporting Information Figure S4). The robustness of our plasmene sheets allows one to use them as mechanical membrane resonators with fundamental resonance frequencies ranging from 40 to 220 kHz. The measured quality factors of such resonators exceeded 100 in air, which is about 1 order of magnitude larger than the quality factors of alkyl-nanoparticle superlattice sheets[34] (see Supporting Information Figure S5).

The NC-based plasmene sheets exhibit strong plasmonic resonance peaks in the extinction spectra. High-precision numerical simulations are then carried out to identify the dominant plasmon modes corresponding to the extinction peaks. The structural parameters of the plasmene sheet were extracted from the representative TEM images (Figure 2a) and used in numerical simulations based on CST Microwave Studio Suite. Figure 2b depicts the near-field distribution pattern calculated along the *z*-plane passing through the center of the NC plasmene sheet. Strong electromagnetic fields are seen to be highly localized in the inter-nanoparticle gaps. A direct correlation can be observed where narrower gaps led to stronger filed confinement. This localized near-field gets enhanced due to the plasmonic coupling between the nanoparticles, and the plasmonic gap resonance arises from the standing wave mode sustained by the capacitive

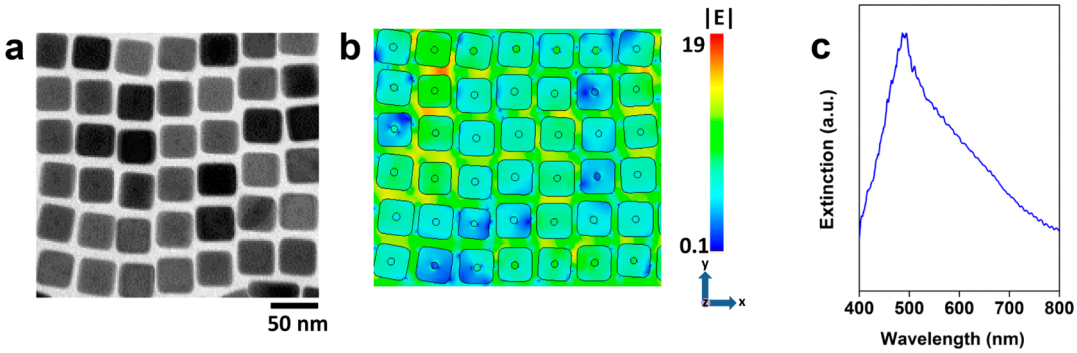

Figure 2. Plasmonic properties of giant NC-plasmene nanosheet. (a) Representative TEM image for NC plasmene sheet used to simulate (b) near-field distributions when excited with light having a free space wavelength of 490 nm. (c) Experimental extinction spectrum of the NC plasmene sheet.

coupling between the adjacent nanoparticles.[35] The observed peak in the extinction spectrum (Figure 2c) corresponds to the resonance of the gap plasmons confined to 2D planes.

In addition to gap plasmon modes, our plasmene sheets could also support plasmon propagating on their top surfaces. We extracted the exact size distribution and interparticle spacing from the TEM image in Figure 2a, and used the ensemble as a unit cell to form a 2D giant plasmene sheet. Simulation shows that when light from an excitation port falls over a small area in the center of the sheet, plasmon excitation can propagate across the entire sheet following a cylindrical wave pattern (see Supporting Information Figure S6, Supporting Information Movies 1 and 2). Numerically calculated field-amplitude decay time of the plasmon excitations provides additional evidence of decaying surface plasmon resonances with 1/e−amplitude decay time of ∼11 fs (see Supporting Information Figure S7), which is significantly longer than the decay time of localized surface plasmons of isolated metal nanoparticles[36] (∼6 fs) and is comparable to the reported value for a nanocrystal superlattice.[35]

To further verify the propagating nature of the excited plasmons, we transferred the plasmene nanosheets onto side-polished D-shape optical fiber to form a hybrid fiber-to-plasmene waveguide coupler (see Supporting Information Figure S8). By investigating the polarization of the output light from this coupler, we were able to determine the nature of the propagating surface wave. Unlike graphene, which supports transverse electric (TE) propagating waves,[37−39] our plasmene sheets selectively support transverse magnetic (TM) propagating waves, with electric field perpendicular to the sheet's surface. This is because the fiber-to-plasmene coupler has a metal−dielectric interface where TE surface wave is forbidden and only the vertically polarized plasmons can propagate through the plasmene sheet (see Supporting Information Figure S9). We obtained a polarization extinction ratio exceeding 10 dB, which is comparable to that of the solid metal film-based polarizers.[40]

Analogous to graphene, our plasmene sheets could be milled into free-standing nanoribbons without any fracture by FIB lithography (Figure 3a−e). We fabricated 3-, 4-, 6-, 8-, and 11-particle-wide NC plasmene nanoribbons, corresponding to widths of 113 ± 10, 206 ± 8, 305 ± 8, 405 ± 8, and 502 ± 11 nm, respectively. All the nanoribbons had smooth top surfaces and the NC particles remained ordered after FIB milling. Both theoretical and experimental results (Figure 3f,g) indicated evident width-dependent properties, analogous to plasmonic properties of graphene nanoribbons.[41] From the simulated extinction spectra of perfectly ordered NCs arranged in shape of ribbons (Figure 3f), we can identify two main trends similar to those reported for graphene nanoribbons when the ribbon width increases: (1) the main characteristic resonance peaks i, ii, iii (corresponding to edge-coupled, corner-coupled and edge-corner-coupled modes, respectively; see Supporting Information Figure S11) exhibited an overall trend of red-shift with increasing ribbon width but at different dispersion rates (Figure 3f). Peak iii disperses a faster rate than peaks i and ii and, hence, exhibits the most prominent red-shift, and (2) the peak iii intensity of the extinction spectra was observed to grow linearly with increasing nanoribbon width (Figure 3g). Note that each extinction spectrum also exhibits a few more low energy peaks/shoulders. The origin of all these spectral features are thoroughly investigated using electric field-lines pattern (see Supporting Information Section II-2 and Figure S12). This helps one to identify the modes based on symmetric/antisymmetric types of coupling between different linear chains of NCs in a plasmene nanoribbon across its width, and the way these modes evolve for wider nanoribbons.

For the experimental spectra, the size dispersions of the constituent nanoparticles and interparticle spacing dispersions resulted in the merging of the weak peaks (peaks i and ii) with the strong peak iii. This can be appreciated from the fact that due to minor disordering present in the fabricated nanoribbons, the edge-coupled mode (peak i) and corner-coupled mode (peak ii)

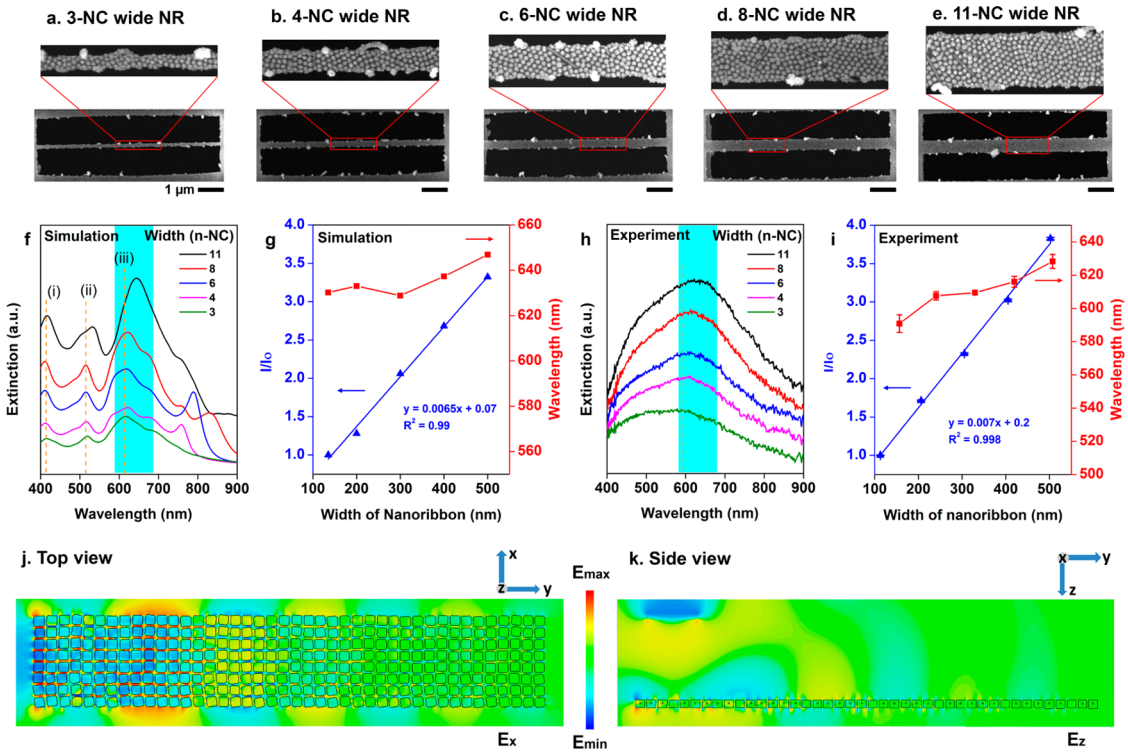

Figure 3. Characterization of plasmene nanoribbons (NRs) with different widths. (a–e) SEM characterization of plasmene nanoribbons with width of (a) ~3, (b) 4, (c) 6, (d) 8, and (e) 11 NCs. (f) Simulated extinction spectra of the nanoribbons from (a–e) and (g) trends of peak (iii) observed in (f) with increasing nanoribbon width. Simulations are based on approximations that all NCs are identical and uniformly spaced. (h) Experimental extinction spectra of the nanoribbons from (a–e) and (i) trends of the dominant peak observed in (h) with increasing nanoribbon width. Highlighted regions indicate the dominant peak considered to investigate the effect of nanoribbon width on its optical response. (j) Top view and (k) side view of electric field distribution along the nanoribbon length (8-NC wide with length of ~1.83 μm) showing the propagation of surface plasmons in form of waveguide mode and edge plasmon mode, when excited with light having a free space wavelength of 490 nm. The simulation is based on exact modeling of NC nanoribbon according to the representative TEM images of NC plasmene sheet shown in Figure 2a.

essentially merge to the edge-corner coupled mode (peak iii), giving rise to a wide spectrum. Moreover, due to the deviation from a perfectly ordered array as considered in simulation, the intensities of the weak low energy modes are more likely to get further reduced, and hence, they do not appear prominently in the experimental spectrum. All these eventually give rise to a broadband extinction spectrum with just one dominant peak, which is recorded experimentally. However, it is noteworthy that despite these imperfections, the trends in the peak developments (Figure 3i) are consistent with those predicted by simulations (Figure 3g), especially for the dominant peak (peak iii).

The width-dependent nanoribbon plasmonic properties can be theoretically interpreted by invoking the well-known plasmon hybridization theory.[28] The extinction resonance peak depends significantly on the strength of the bonding plasmons between NCs. The plasmon hybridization theory predicts that the resonant energy of the bonding plasmons is lower than that of discrete plasmons, leading to a spectral red shift. With increase in nanoribbon width, more number of bonding plasmons interact with each other, therefore, leading to spectral red-shift of the extinction peak.

To estimate the plasmon propagation length in a nanoribbon, we modeled a 1D NC-plasmene nanoribbon using a unit cell based on the representative TEM image (Figure 2a) by repeating the unit cell unidirectionally. The excitation port impinges light over a small area on one end of the nanoribbon, creating plasmons propagating along the length of the nanoribbon. Simulations predicted a 1/e–amplitude decay propagating length of ~340 nm when excited with light at the gap-mode-resonance wavelength of 490 nm. This propagation length can be further increased by impinging light with shorter wavelength as losses in silver monotonously decreases with shorter wavelength. Similar to graphene nanoribbons,[42] waveguide mode and edge mode surface plasmon propagation can be observed for our plasmene nanoribbons, as seen in top view (Figure 3j, see Supporting Information Movie 3) and side view (Figure 3k, see Supporting Information Movie 4).

Remarkably, our unique plasmene nanosheets could be folded into various geometrically well-defined 3D origamis by programmed FIB-milling. The "gentle" FIB milling can partially etch the sheets, likely by removing the surface-binding polystyrene ligands and induce

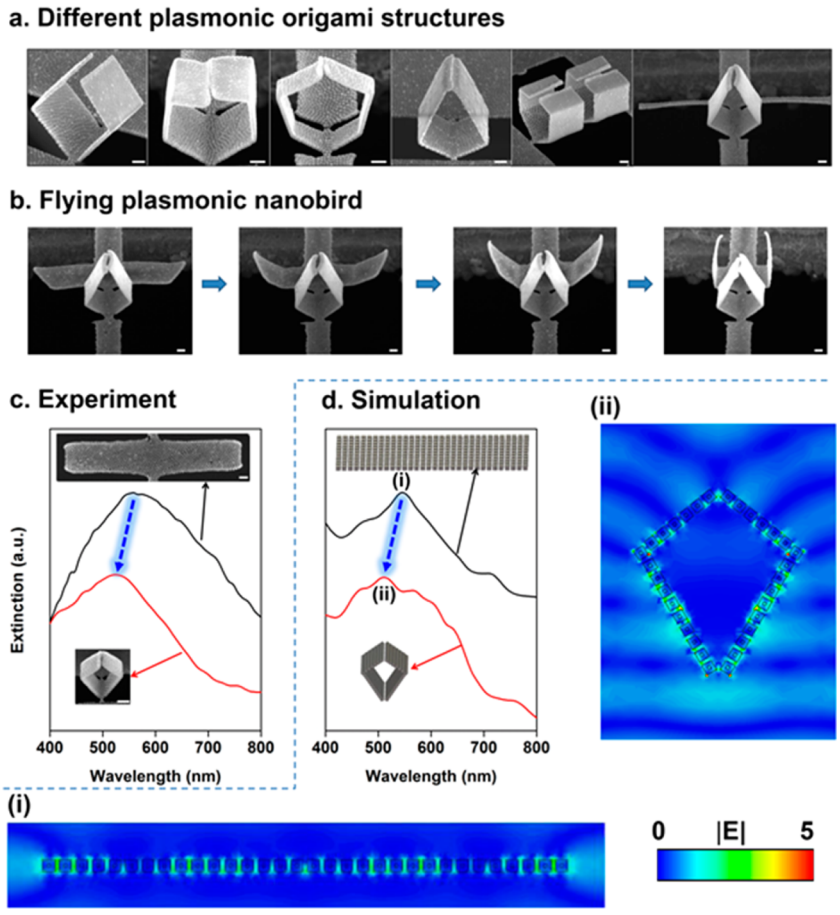

Figure 4. Plasmene origami. (a) SEM images showing the different origami structures: cube, pentagon, hexagon, diamond, hearts, and plane. (b) A series of SEM images depicting the flapping motion of a bird's wings. (c) Experimental and (d) simulation spectra for unfolded sheet and folded 3D origami structure. Insets in (c) and (d) show SEM images and simulation models of the corresponding structures, respectively. Normalized near-field distribution patterns along the cross sections of the simulation models for the peaks (i) and (ii), shown in the simulation spectra. Scale bar is 200 nm for all SEM images.

local heating,[43] which resulted in local stress buildup and folding of plasmene sheets at certain angles depending on the milling depth (see Supporting Information Figure S13). By programming the FIB-milling parameters including locations, beam current and dwelling time (see Supporting Information Section III-2), we could obtain well-defined origami structures such as cube, hexagon, pentagon, heart, air plane (Figure 4a), and even a "flying bird" (Figure 4b, see Supporting Information Movie 5). The folding angles of the bird wings can be well-controlled by programming the milling depth.

Using the 3D origami structure (shown in the inset of Figure 4c) as an example, we illustrate how folding affects plasmonic resonance properties. We found that plasmonic peak shifted to blue with narrowing bandwidth when unfolded nanoribbon was crafted into a 3D origami. Consistent with experimental observations (Figure 4c), the numerical simulations also predicted blue shift with folding (Figure 4d). The blue shift may be attributed to reduction in plasmonic interactions owing to incoherent interparticle coupling between the nanocubes of the origami structure. This may be attributed to the fact that for an origami structure, incident light reaches the nanoparticles (at different heights) of the side planes of the 3D origami at different phases. The near-field distribution patterns obtained along the cross section of an unfolded nanoribbon (Figure 4d (i)) and folded 3D origami (Figure 4d (ii)) also testify the change in near-field coupling between adjacent nanocubes of the ribbon upon folding.

The effect of folding of a plasmene nanoribbon on its optical response is further investigated by numerically evaluating the extinction spectra of single-folded ribbons with different folding angles (see Supporting Information Section III-3). The trend of spectral evolution of plasmon resonance peaks with increasing folding angles is shown in Supporting Information Figure S20. A comparative analysis of the normalized near-field distribution patterns (see Supporting Information Figures S21 and S22) allow one to appreciate folding-induced spectral evolution of the dominant resonance peak. On the basis of these findings, we analyzed and explained the blue shift in the evolution of optical spectrum for a multifolded 3D origami shown in

Figure 4d (see Supporting Information Section III-3 and Figure S23). Although, some minor differences were noted between the simulated and experimental spectra, these can be attributed to the fact that all the NCs are considered to be identical and uniformly spaced in the simulations (see Supporting Information Figure S23).

CONCLUSION

In summary, we have demonstrated a robust general approach to fabricate giant plasmene nanosheets which exhibit analogous properties to graphene as well as some unique features. Similar to graphene, our plasmene is mechanically robust, and can be used as a mechanical resonator; it can also support propagating plasmons and be shaped into 1D nanoribbons with width-dependent plasmonic properties. Despite their structural imperfection, our first version of plasmene sheets have exhibited a number of unique features: (1) plasmene could be, in principle, customized arbitrarily using various "meta-atoms" elements from the artificial metamaterial periodic table;[29] (2) the hybrid organic/inorganic composition of our plasmene sheets enabled the fabrication of 3D origami structures. Given the generality of the concepts and methodologies established here, we believe that plasmene materials will lead to a wide range of scientific and technological applications, like flexible and stretchable plasmonics, foldable plasmonic devices, plasmonic waveguiding, switching and sensing, *etc*.

METHODS

Materials. Gold(III) chloride trihydrate ($HAuCl_4 \cdot 3H_2O$, ≥99.9%), hexadecyltrimethylammonium bromide (CTAB), cetyltrimethylammonium chloride solution (CTAC, 25 wt % in H_2O), silver nitrate ($AgNO_3$), sodium borohydride ($NaBH_4$) and L-ascorbic acid were purchased from Sigma-Aldrich. Tetrahydrofuran (THF) and chloroform were obtained from Merck KGaA. Thiol-functionalized polystyrene (M_n = 50 000 g/mol, M_w/M_n = 1.06) was purchased from Polymer Source, Inc. All chemicals were used as-received unless otherwise indicated. Demineralized water was used in all aqueous solutions, which were further purified with a Milli-Q system (Millipore). All glassware used in the following procedures was cleaned in a bath of freshly prepared *aqua regia* and rinsed thoroughly in H_2O prior to use.

Gilder extra fine bar grids (2000 mesh with 7 × 7 μm^2 square holes) were purchased from Ted Pella. Holey silicon nitride support films (2-μm-diameter hole, 4 μm pitch) were purchased from SPI supplies.

Synthesis of Polystyrene-Capped Au@Ag NCs. The synthesis of high-quality CTAC-capped Au@Ag NCs was achieved by adopting the slightly modified recently developed approaches[32] (see Supporting Information Section I-1). Replacement of CTAC with thiolated PS was achieved using a two-step ligand-exchange procedure.[27,31] The as-prepared CTAC-stabilized Au@Ag NCs (5 mL) were typically spun down and concentrated into 0.1 mL, followed by dropwise addition of the above concentrated Au@Ag NCs to an excess thiol-functionalized polystyrene solution (dissolved in THF, 2 mg mL^{-1}) under vigorous stirring. After aging overnight at room temperature, the supernatant was discarded and the samples were purified by repeated centrifugation–precipitation cycles and redispersed in chloroform as a stock solution.

Fabrication of Giant Plasmene Nanosheet. One drop of chloroform solution of PS-capped Au@Ag NCs (~27 nM) was typically spread onto the surface of convex-shape water droplet on a holey copper or silicon nitride grid. After quick chloroform evaporation, silver-colored reflective solid films formed on the water subphase. Subsequently, water slowly evaporated, leading to the formation of the giant plasmene sheets that covered almost the entire grid.

Fabrication of Nanoribbons and Origami. Plasmene sheet on a holey copper grid (7 μm × 7 μm) was bonded to ITO glass on an aluminum sample holder with conductive copper tape to eliminate any charging effect. FEI Helios Nanolab 600 FIB machine was used to generate gallium ions with an accelerating voltage of 30 kV. An ion beam current of 28 pA and a dwell time of 100 μs/100 ns were used in the experiments. The detailed patterning design and dimensions are given in the Supporting Information Section II and III.

Characterization. Electron imaging was carried out using Philips CM20 TEM or FEI Tecnai G2 T20 TEM operating at an accelerating voltage of 200 kV, or Hitachi H-7500 field emission TEM operating at 80 kV.

The optical extinction spectra of the bulk solution samples were measured using Agilent 8453 UV–vis spectrophotometer and the spectra of plasmene nanosheets, nanoribbons and origamis were obtained using J&M MSP210 microscope spectrometry system. Optical micrographs of the plasmene sheets were taken by Nikon industrial bright-field microscope (ECLIPSE LV 100D) under transmission and reflectance modes.

Mechanical properties were measured by adopting the previously reported approach.[16] Force–displacement curves and topographical structures were obtained with a Veeco Dimension Icon AFM in tapping mode using Bruker silicon probes (MPP-11120-10). The spring constant of the cantilever was 40 N m^{-1}. The typical tip speed for the nanoindentation was 500 nm s^{-1}. The AFM data was characterized using Gwyddion software.

Resonance properties were collected by mounting a piezoelectric transducer (PZT) plate driven by an electrical function generator on the backside of the membrane chip. The vibration displacement amplitude of the membrane resonator was measured by PolyTec interferometer with phase locked loop, which has a picometer resolution in vibration amplitude. During standing wave vibration amplitude 2D mapping, the driving frequency was fixed at the resonance mode and the interferometer laser gun was controlled by a stage controller for lateral movement with sub-0.5 μm lateral resolution.

Numerical Simulations. The numerical simulations of plasmene nanoribbon and origami structures were performed using CST Microwave Studio Suite. The frequency–domain FEM solver was deployed to obtain the extinction spectra of these nanostructures. Perfectly matched layer (PML) was used at the simulation domain boundaries, making the incident waves pass the boundaries with minimal reflections. Some extra space was also added in the models around the target nanostructure within the open boundaries to enable far-field calculations. Tetrahedral mesh, which is more accurate at metallic material interfaces, was used in the frequency–domain simulations with automatic mesh refinement to study the optical response over the wavelength window of interest. An adaptive hexahedral meshing was considered for time–domain simulations. Steady-state accuracy limit of −60 dB was considered in all the time–domain studies reported here.

Conflict of Interest: The authors declare no competing financial interest.

Supporting Information Available: Detailed description of the experimental procedures and theoretical simulations employed for this work; movies of plamene sheets, nanoribbons, and origami structures (.zip). This material is available free of charge *via* the Internet at http://pubs.acs.org.

Acknowledgment. M.P., W.Z., and W.L.C. acknowledge Discovery Grants DP110100713, DP140100883, DP120100170, and DP140100052. This work was performed in part at the Melbourne Centre for Nanofabrication (MCN) in the Victorian Node of the Australian National Fabrication Facility (ANFF). We thank Ivan D. Rukhlenko for suggestions in modeling and Fatemeh Eftekhari for the technical support in focused ion beam lithography. The authors also gratefully acknowledge the use of facilities at Monash Micro Imaging Centre. The work of D.S. is supported by the DSDBI of the Victorian Government, through its Victoria India Doctoral Scholarship Program (managed by the Australia India Institute). Q.B. acknowledges the support from 863 Program (2013AA031903), the NSFC Grants (51222208, 51290273), ARC DECRA (DE120101569), DP (DP140101501).

Note Added after ASAP Publication: This paper published ASAP on October 2, 2014. An important author was added and the revised version was reposted on November 5, 2014.

REFERENCES AND NOTES

1. Tang, Z.; Zhang, Z.; Wang, Y.; Glotzer, S. C.; Kotov, N. A. Self-Assembly of CdTe Nanocrystals into Free-Floating Sheets. *Science* **2006**, *314*, 274–278.
2. Redl, F. X.; Cho, K. S.; Murray, C. B.; O'Brien, S. Three-Dimensional Binary Superlattices of Magnetic Nanocrystals and Semiconductor Quantum Dots. *Nature* **2003**, *423*, 968–971.
3. Kotov, N. A.; Meldrum, F. C.; Wu, C.; Fendler, J. H. Monoparticulate Layer and Langmuir-Blodgett-Type Multiparticulate Layers of Size-Quantized Cadmium Sulfide Clusters: A Colloid-Chemical Approach to Superlattice Construction. *J. Phys. Chem.* **1994**, *98*, 2735–2738.
4. Talapin, D. V.; Shevchenko, E. V.; Bodnarchuk, M. I.; Ye, X.; Chen, J.; Murray, C. B. Quasicrystalline Order in Self-Assembled Binary Nanoparticle Superlattices. *Nature* **2009**, *461*, 964–967.
5. Dong, A. G.; Chen, J.; Vora, P. M.; Kikkawa, J. M.; Murray, C. B. Binary Nanocrystal Superlattice Membranes Self-Assembled at the Liquid-Air Interface. *Nature* **2010**, *466*, 474–477.
6. Freeman, R. G.; Grabar, K. C.; Allison, K. J.; Bright, R. M.; Davis, J. A.; Guthrie, A. P.; Hommer, M. B.; Jackson, M. A.; Smith, P. C.; Walter, D. G.; *et al.* Self-Assembled Metal Colloid Monolayers: An Approach to SERS Substrates. *Science* **1995**, *267*, 1629–1632.
7. Whetten, R. L.; Khoury, J. T.; Alvarez, M. M.; Murthy, S.; Vezmar, I.; Wang, Z. L.; Stephens, P. W.; Cleveland, C. L.; Luedtke, W. D.; Landman, U. Nanocrystal Gold Molecules. *Adv. Mater.* **1996**, *8*, 428–433.
8. Collier, C. P.; Saykally, R. J.; Shiang, J. J.; Henrichs, S. E.; Heath, J. R. Reversible Tuning of Silver Quantum Dot Monolayers through the Metal-Insulator Transition. *Science* **1997**, *277*, 1978–1981.
9. Kiely, C. J.; Fink, J.; Brust, M.; Bethell, D.; Schiffrin, D. J. Spontaneous Ordering of Bimodal Ensembles of Nanoscopic Gold Clusters. *Nature* **1998**, *396*, 444–446.
10. Courty, A.; Mermet, A.; Albouy, P. A.; Duval, E.; Pileni, M. P. Vibrational Coherence of Self-Organized Silver Nanocrystals in f.c.c. Supra-Crystals. *Nat. Mater.* **2005**, *4*, 395–398.
11. Tao, A.; Sinsermsuksakul, P.; Yang, P. Tunable Plasmonic Lattices of Silver Nanocrystals. *Nat. Nanotechnol.* **2007**, *2*, 435–440.
12. Henzie, J.; Grünwald, M.; Widmer-Cooper, A.; Geissler, P. L.; Yang, P. Self-Assembly of Uniform Polyhedral Silver Nanocrystals into Densest Packings and Exotic Superlattices. *Nat. Mater.* **2012**, *11*, 131–137.
13. Cheng, W. L.; Hartman, M. R.; Smilgies, D. M.; Long, R.; Campolongo, M. J.; Li, R.; Sekar, K.; Hui, C. Y.; Luo, D. Probing in Real Time the Soft Crystallization of DNA-Capped Nanoparticles. *Angew. Chem., Int. Ed.* **2010**, *49*, 380–384.
14. Park, S. Y.; Lytton-Jean, A. K. R.; Lee, B.; Weigand, S.; Schatz, G. C.; Mirkin, C. A. DNA-Programmable Nanoparticle Crystallization. *Nature* **2008**, *451*, 553–556.
15. Nykypanchuk, D.; Maye, M. M.; van der Lelie, D.; Gang, O. DNA-Guided Crystallization of Colloidal Nanoparticles. *Nature* **2008**, *451*, 549–552.
16. Cheng, W. L.; Campolongo, M. J.; Cha, J. J.; Tan, S. J.; Umbach, C. C.; Muller, D. A.; Luo, D. Free-Standing Nanoparticle Superlattice Sheets Controlled by DNA. *Nat. Mater.* **2009**, *8*, 519–525.
17. Mueggenburg, K. E.; Lin, X. M.; Goldsmith, R. H.; Jaeger, H. M. Elastic Membranes of Close-Packed Nanoparticle Arrays. *Nat. Mater.* **2007**, *6*, 656–660.
18. Korgel, B. A. Nanocrystal Superlattices Assembly at Liquid Interfaces. *Nat. Mater.* **2010**, *9*, 701–703.
19. Auyeung, E.; Cutler, J. I.; Macfarlane, R. J.; Jones, M. R.; Wu, J.; Liu, G.; Zhang, K.; Osberg, K. D.; Mirkin, C. A. Synthetically Programmable Nanoparticle Superlattices Using a Hollow Three-Dimensional Spacer Approach. *Nat. Nanotechnol.* **2012**, *7*, 24–28.
20. Bigioni, T. P.; Lin, X. M.; Nguyen, T. T.; Corwin, E. I.; Witten, T. A.; Jaeger, H. M. Kinetically Driven Self Assembly of Highly Ordered Nanoparticle Monolayers. *Nat. Mater.* **2006**, *5*, 265–270.
21. Gong, J.; Li, G.; Tang, Z. Self-Assembly of Noble Metal Nanocrystals: Fabrication, Optical Property, and Application. *Nano Today* **2012**, *7*, 564–585.
22. Zhu, Z.; Meng, H.; Liu, W.; Liu, X.; Gong, J.; Qiu, X.; Jiang, L.; Wang, D.; Tang, Z. Superstructures and SERS Properties of Gold Nanocrystals with Different Shapes. *Angew. Chem., Int. Ed.* **2011**, *50*, 1593–1596.
23. Ming, T.; Kou, X.; Chen, H.; Wang, T.; Tam, H. L.; Cheah, K. W.; Chen, J. Y.; Wang, J. Ordered Gold Nanostructure Assemblies Formed By Droplet Evaporation. *Angew. Chem., Int. Ed.* **2008**, *47*, 9685–9690.
24. Kostiainen, M. A.; Hiekkataipale, P.; Laiho, A.; Lemieux, V.; Seitsonen, J.; Ruokolainen, J.; Ceci, P. Electrostatic Assembly of Binary Nanoparticle Superlattices Using Protein Cages. *Nat. Nanotechnol.* **2013**, *8*, 52–56.
25. Ye, X.; Chen, J.; Diroll, B. T.; Murray, C. B. Tunable Plasmonic Coupling in Self-Assembled Binary Nanocrystal Superlattices Studied by Correlated Optical Microspectrophotometry and Electron Microscopy. *Nano Lett.* **2013**, *13*, 1291–1297.
26. Chen, C. F.; Tzeng, S. D.; Chen, H. Y.; Lin, K. J.; Gwo, S. Tunable Plasmonic Response from Alkanethiolate-Stabilized Gold Nanoparticle Superlattices: Evidence of Near-Field Coupling. *J. Am. Chem. Soc.* **2007**, *130*, 824–826.
27. Ng, K. C.; Udagedara, I. B.; Rukhlenko, I. D.; Chen, Y.; Tang, Y.; Premaratne, M.; Cheng, W. L. Free-Standing Plasmonic-Nanorod Superlattice Sheets. *ACS Nano* **2011**, *6*, 925–934.
28. Prodan, E.; Radloff, C.; Halas, N. J.; Nordlander, P. A Hybridization Model for the Plasmon Response of Complex Nanostructures. *Science* **2003**, *302*, 419–422.
29. Tan, S. J.; Campolongo, M. J.; Luo, D.; Cheng, W. L. Building Plasmonic Nanostructures with DNA. *Nat. Nanotechnol.* **2011**, *6*, 268–276.
30. Huang, F. M.; Sinha, J. K.; Gibbons, N.; Bartlett, P. N.; Baumberg, J. J. Direct Assembly of Three-Dimensional Mesh Plasmonic Rolls. *Appl. Phys. Lett.* **2012**, *100*, 193107.
31. Chen, Y.; Fu, J.; Ng, K. C.; Tang, Y.; Cheng, W. L. Free-Standing Polymer-Nanoparticle Superlattice Sheets Self-Assembled at the Air Liquid Interface. *Cryst. Growth Des.* **2011**, *11*, 4742–4746.
32. Ma, Y.; Li, W.; Cho, E. C.; Li, Z.; Yu, T.; Zeng, J.; Xie, Z.; Xia, Y. Au@Ag Core−Shell Nanocubes with Finely Tuned and Well-Controlled Sizes, Shell Thicknesses, and Optical Properties. *ACS Nano* **2010**, *4*, 6725–6734.
33. Gong, J.; Zhou, F.; Li, Z.; Tang, Z. Synthesis of Au@Ag Core−Shell Nanocubes Containing Varying Shaped Cores and Their Localized Surface Plasmon Resonances. *Langmuir* **2012**, *28*, 8959–8964.
34. Kanjanaboos, P.; Lin, X. M.; Sader, J. E.; Rupich, S. M.; Jaeger, H. M.; Guest, J. R. Self-Assembled Nanoparticle Drumhead Resonators. *Nano Lett.* **2013**, *13*, 2158–2162.
35. Tao, A. R.; Ceperley, D. P.; Sinsermsuksakul, P.; Neureuther, A. R.; Yang, P. Self-Organized Silver Nanoparticles for Three-Dimensional Plasmonic Crystals. *Nano Lett.* **2008**, *8*, 4033–4038.

36. Lamprecht, B.; Krenn, J. R.; Leitner, A.; Aussenegg, F. R. Resonant and Off-Resonant Light-Driven Plasmons in Metal Nanoparticles Studied by Femtosecond-Resolution Third-Harmonic Generation. *Phys. Rev. Lett.* **1999**, *83*, 4421–4424.
37. Bao, Q.; Zhang, H.; Wang, B.; Ni, Z.; Lim, C. H. Y. X.; Wang, Y.; Tang, D. Y.; Loh, K. P. Broadband Graphene Polarizer. *Nat. Photonics* **2011**, *5*, 411–415.
38. Jablan, M.; Buljan, H.; Soljačić, M. Plasmonics in Graphene at Infrared Frequencies. *Phys. Rev. B* **2009**, *80*, 245435.
39. Mikhailov, S. A.; Ziegler, K. New Electromagnetic Mode in Graphene. *Phys. Rev. Lett.* **2007**, *99*, 016803.
40. Eickhoff, W. In-Line Fibre-Optic Polariser. *Electron. Lett.* **1980**, *16*, 762–764.
41. Yan, H.; Low, T.; Zhu, W.; Wu, Y.; Freitag, M.; Li, X.; Guinea, F.; Avouris, P.; Xia, F. Damping Pathways of Mid-Infrared Plasmons in Graphene Nanostructures. *Nat. Photonics* **2013**, *7*, 394–399.
42. Wang, J.; Lu, W. B.; Li, X. B.; Ni, Z. H.; Qiu, T. Graphene Plasmon Guided Along a Nanoribbon Coupled with a Nanoring. *J. Phys. D: Appl. Phys.* **2014**, *47*, 135106.
43. Lee, C. C.; Proust, G.; Alici, G.; Spinks, G. M.; Cairney, J. M. Three-Dimensional Nanofabrication of Polystyrene by Focused Ion Beam. *J. Microsc.* **2012**, *248*, 129–139.